Electronic Supplementary Material (ESI) for Dalton Transactions.
This journal is © The Royal Society of Chemistry 2020

Electronic Supplementary Information (ESI) for Dalton Transactions,

This journal is © The Royal Society of Chemistry 2020

Electronic Supplementary Information (ESI):

The first pentagonal-bipyramidal vanadium (III) complexes with a Schiff-base N_3O_2 pentadentate ligand: synthesis, structure and magnetic properties

T.A. Bazhenova[a], L.V. Zorina[b], S.V. Simonov[b], V.S. Mironov[a,c], O.V. Maximova[a,d,e], L. Spillecke[f], C. Koo[f], R. Klingeler[f,g], Yu.V. Manakin[a],A.N. Vasiliev[d,h], and E.B. Yagubskii[a]

[a]Institute of Problems of Chemical Physics, RAS, Chernogolovka 142432, Russia

[b]Institute of Solid State Physics, RAS, Chernogolovka 142432, Russia

[c]Shubnikov Institute of Crystallography of Federal Scientific Research Centre "Crystallography and Photonics", RAS, Moscow, Russia

[d]Lomonosov Moscow State University, Moscow 119991, Russia.

[e]National University of Science and Technology "MISiS", Moscow 119049, Russia

[f]Kirchhoff Institute for Physics, Heidelberg University, 69120 Heidelberg, Germany

[g]Centre for Advanced Materials (CAM), Heidelberg University, 69120 Heidelberg, Germany

[h]National Research South Ural State University, Chelyabinsk 454080, Russia

Supporting Information

CONTENT:

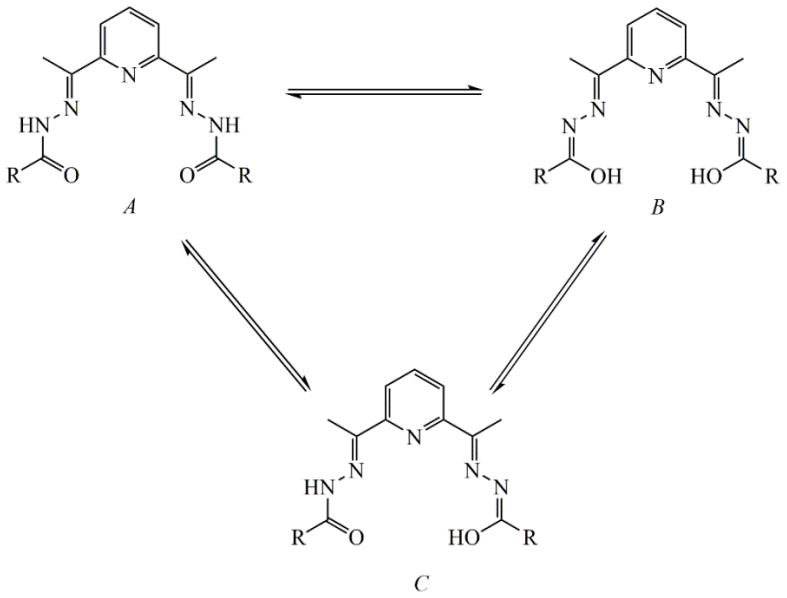

Figure S1. Three isomeric forms in solution of the 2,6-diacetylpyridine-based acyclic ligands. R = NH_2 (H_2DAPSC), 2-OHC_6H_4 (H_4DAPS) and C_6H_5 (H_2DAPBH); the latter ligand is used in this work.

X-ray structures and hydrogen bond geometry in 1-3

[V(H_2DAPBH)Cl_2]Cl·EtOH (**1**)

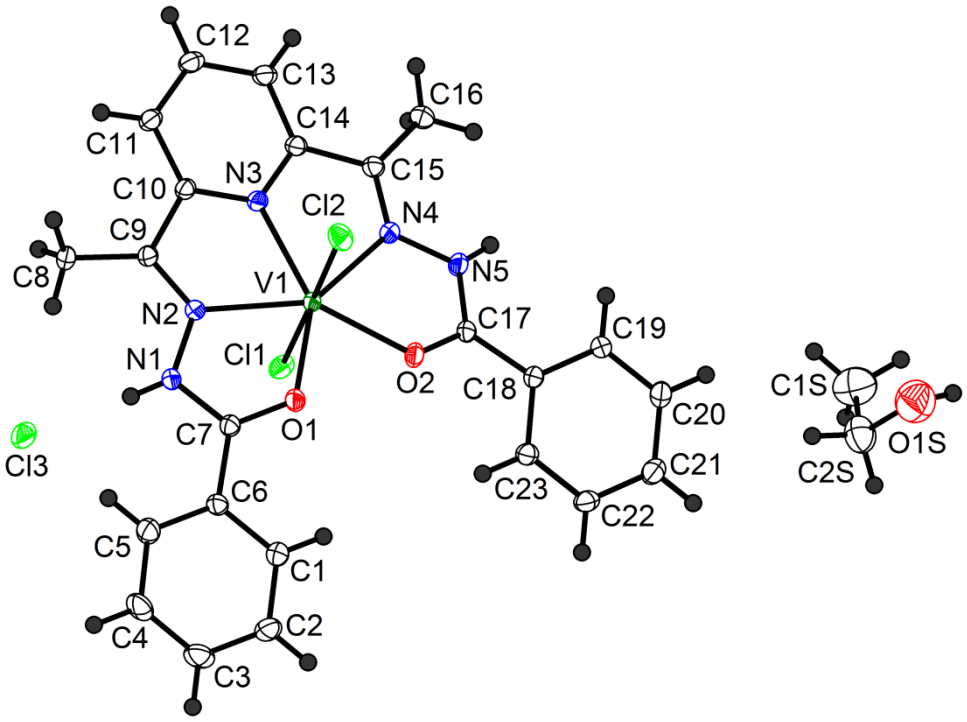

Figure S2. Asymmetric unit with atom numbering scheme in **1** (50% thermal ellipsoids).

Table S1. Selected bond lengths (Å) and angles (º) in **1**.

V1-O1	2.059(2)	O1-C7	1.249(2)	O2-C17	1.249(2)
V1-O2	2.061(1)	C7-N1	1.352(3)	C17-N5	1.348(3)
V1-N2	2.140(2)	N1-N2	1.378(2)	N5-N4	1.371(2)
V1-N4	2.153(2)	N2-C9	1.292(2)	N4-C15	1.293(2)
V1-N3	2.128(2)	C9-C10	1.476(3)	C15-C14	1.474(3)
V1-Cl1	2.3629(6)	C10-N3	1.347(3)	C14-N3	1.343(3)
V1-Cl2	2.3927(6)				

O1-V1-N2	72.03(6)	O2-V1-N4	71.98(6)
O1-V1-N3	142.48(6)	O2-V1-N3	142.62(7)
O1-V1-N4	146.75(6)	O2-V1-N2	146.45(6)
N2-V1-N3	70.87(6)	N4-V1-N3	70.75(6)
O1-V1-O2	74.78(6)	N2-V1-N4	140.92(6)
O1-V1-Cl1	87.80(5)	O2-V1-Cl1	88.25(5)
N2-V1-Cl1	85.75(5)	N4-V1-Cl1	90.38(5)
O1-V1-Cl2	91.35(5)	O2-V1-Cl2	92.43(5)
N2-V1-Cl2	93.09(5)	N4-V1-Cl2	90.84(5)
N3-V1-Cl1	94.88(5)	N3-V1-Cl2	85.23(5)
Cl1-V1-Cl2	178.73(2)		

The V(III) complexes in **1** form layers parallel to the *ab* plane (Fig. S3). The chlorine anions are located in between the layers. Average planes of H_2DAPBH ligands are not parallel both within the layer and in adjacent layers along the *c*-axis (the corresponding dihedral angles between the VN_3O_2 planes are 29.76(3) and 54.19(3)º, respectively). The $[V(H_2DAPBH)Cl_2]^+$ cations are connected through the hydrogen bonding. There are $N\text{-}H_{H2DAPBH}\cdots O\text{-}H_{EtOH}\cdots Cl_{ligand}$ hydrogen bonds within the layers along *a* and $N\text{-}H_{H2DAPBH}\cdots Cl_{anion}\cdots H\text{-}N_{H2DAPBH}$ bonds between the layers along *c*. Hydrogen bond geometry is given in Table S2. The nearest V…V distance in the structure **1** is 7.290 Å along *a* between the hydrogen-bonded cations. There are also π-stacking interactions between the adjacent cations in the *ab* layer, corresponding C…C distances less than the sum of van der Waals radii (3.6 Å) are shown in Fig. S3b, the V…V distances are 8.108 and 9.126 Å.

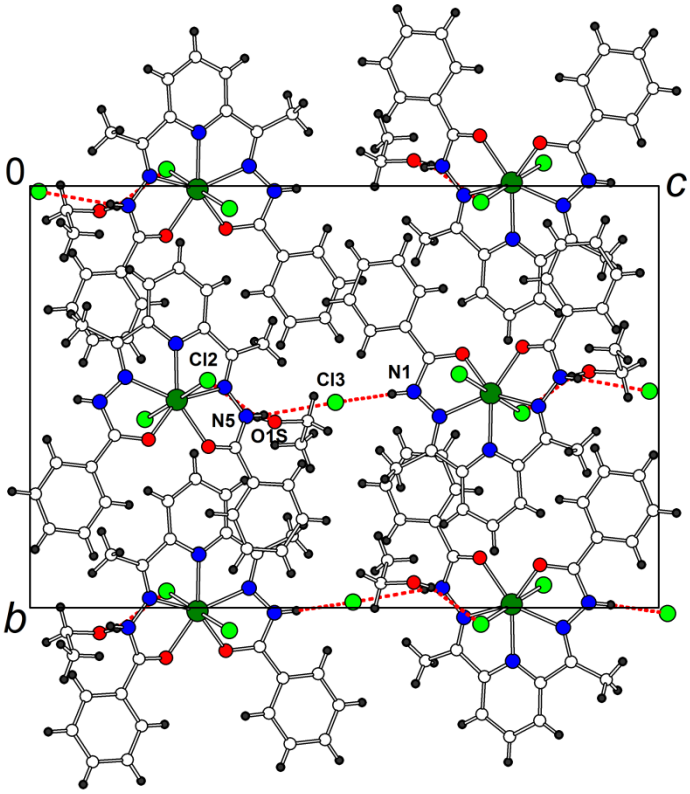

(a)

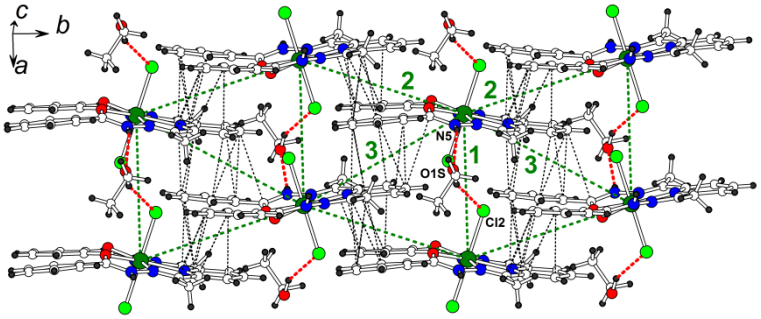

(b)

Figure S3. Projection of the structure **1** along *a* (a). The *ab* layer with hydrogen bonding and π-stacking interactions (b). Hydrogen bonds from acidic H-atoms (red dashed lines), C…C contacts < 3.6 Å (black dotted lines), V…V distances (green dashed lines, 1 = 7.2902(5), 2 = 8.1084(5), 3 = 9.1259(5) Å) are shown.

Table S2. Hydrogen bond geometry in **1**.

D	H	A	Symmetry code for A	D-H, Å	H…A, Å	D…A, Å	D-H…A, º
N1	H1N	Cl3	x, y, z	0.82(2)	2.25(2)	3.0595(17)	171(3)
N5	H5N	Cl3	1.5-x, 2-y, z-0.5	0.81(2)	2.75(2)	3.2920(19)	126(3)
N5	H5N	O1S	x-0.5, 1.5-y, 1-z	0.81(2)	2.19(2)	2.843(4)	137(3)
O1S	H1S	Cl2	x-0.5, 1.5-y, 1-z	0.82	2.35	3.095(3)	152.1
C3	H3	Cl3	x+0.5, 1.5-y, 2-z	0.93	2.72	3.485(2)	140.0
C8	H8A	Cl3	x, y, z	0.96	2.68	3.383(2)	130.5
C11	H11	O1S	1.5-x, 2-y, z+0.5	0.93	2.53	3.239(4)	133.5
C13	H13	Cl1	1-x, y+0.5, 1.5-z	0.93	2.83	3.460(2)	125.9
C16	H16A	Cl3	1.5-x, 2-y, z-0.5	0.96	2.70	3.602(2)	156.0
C19	H19	Cl3	1.5-x, 2-y, z-0.5	0.93	2.64	3.508(2)	156.0
C22	H22	Cl1	1-x, y-0.5, 1.5-z	0.93	2.77	3.409(2)	126.9
C1S	H1SA	Cl3	1-x, y-0.5, 1.5-z	0.96	2.18	3.131(5)	171.2
C1S	H1SB	O2	x-0.5, 1.5-y, 1-z	0.96	2.67	3.605(5)	166.0

[V(HDAPBH)(NCS)$_2$]·0.5MeCN·0.5MeOH (**2**)

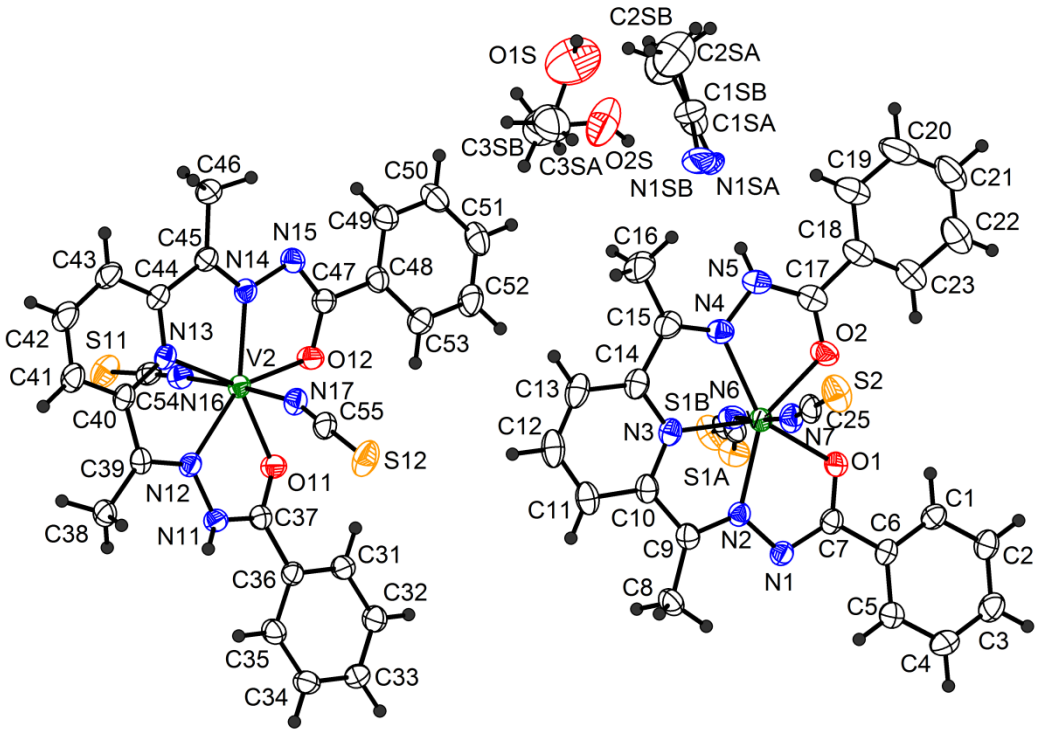

Figure S4. Asymmetric unit with atom numbering scheme in **2** (50% thermal ellipsoids).

Table S3. Selected bond lengths (Å) and angles (º) in **2**.

V1-O1	1.993(2)	O1-C7	1.282(3)	O2-C17	1.239(3)
V1-O2	2.067(2)	C7-N1	1.316(3)	C17-N5	1.350(4)
V1-N2	2.123(2)	N1-N2	1.379(3)	N5-N4	1.379(3)
V1-N4	2.166(2)	N2-C9	1.297(3)	N4-C15	1.295(4)
V1-N3	2.132(2)	C9-C10	1.455(4)	C15-C14	1.479(4)
V1-N6	2.051(3)	C10-N3	1.346(4)	C14-N3	1.343(4)
V1-N7	2.057(3)				

O1-V1-N2	72.47(8)	O2-V1-N4	71.40(8)
O1-V1-N3	143.47(8)	O2-V1-N3	142.22(9)
O1-V1-N4	145.53(8)	O2-V1-N2	146.29(9)
N2-V1-N3	71.43(9)	N4-V1-N3	70.84(9)
O1-V1-O2	74.17(8)	N2-V1-N4	141.97(9)
O1-V1-N6	89.75(9)	O2-V1-N6	89.01(9)
N2-V1-N6	86.11(9)	N4-V1-N6	91.39(9)
O1-V1-N7	90.37(9)	O2-V1-N7	88.42(9)
N2-V1-N7	96.51(9)	N4-V1-N7	86.98(10)
N3-V1-N6	93.19(9)	N3-V1-N7	88.32(9)
N6-V1-N7	177.29(10)		

V2-O11	2.114(2)	O11-C37	1.247(3)	O12-C47	1.282(3)
V2-O12	2.008(2)	C37-N11	1.353(3)	C47-N15	1.316(3)
V2-N12	2.173(2)	N11-N12	1.370(3)	N15-N14	1.377(3)
V2-N14	2.114(2)	N12-C39	1.289(3)	N14-C45	1.297(3)
V2-N13	2.142(2)	C39-C40	1.465(4)	C45-C44	1.464(4)
V2-N16	2.062(3)	C40-N13	1.348(3)	C44-N13	1.346(3)
V2-N17	2.038(3)				

O11-V2-N12	70.82(8)	O12-V2-N14	72.62(8)
O11-V2-N13	140.13(8)	O12-V2-N13	144.16(8)
O11-V2-N14	148.17(8)	O12-V2-N12	145.92(8)
N12-V2-N13	69.84(8)	N14-V2-N13	71.61(8)
O11-V2-O12	75.56(7)	N12-V2-N14	140.88(8)
O11-V2-N16	88.76(9)	O12-V2-N16	91.68(9)
N12-V2-N16	93.00(9)	N14-V2-N16	91.41(9)
O11-V2-N17	88.94(9)	O12-V2-N17	90.73(9)
N12-V2-N17	83.33(9)	N14-V2-N17	92.18(9)
N13-V2-N16	86.98(9)	N13-V2-N17	92.82(9)
N16-V2-N17	176.15(9)		

Projection of the structure **2** along *a* is shown in Fig. S5a. The structure is formed by chains of alternating complexes with V1 and V2 centers. These zigzag chains run along *a*-direction (Fig. S5b). A number of short C…C contacts between V-complexes with distances less than the sum of van der Waals radii (3.6 Å) form intrachain interactions. The NH-functions of HDAPBH ligands are locked on S-atom of the NCS-ligand of the nearest V-complex from adjacent chain or N-atom of the disordered MeCN solvent (Fig. S5a). Also, interchain interactions are formed by short C…C contacts between [V(HDAPBH)$(NCS)_2$] complexes and the hydrogen bonding through solvent molecules. Hydrogen bond geometry is given in Table S4. The nearest V…V distance in the structure **2** is 7.868 and 7.952 Å between the V(1) and V(2) centers along *a* in chain and 8.171, 8.823 Å between chains (Fig. S5c).

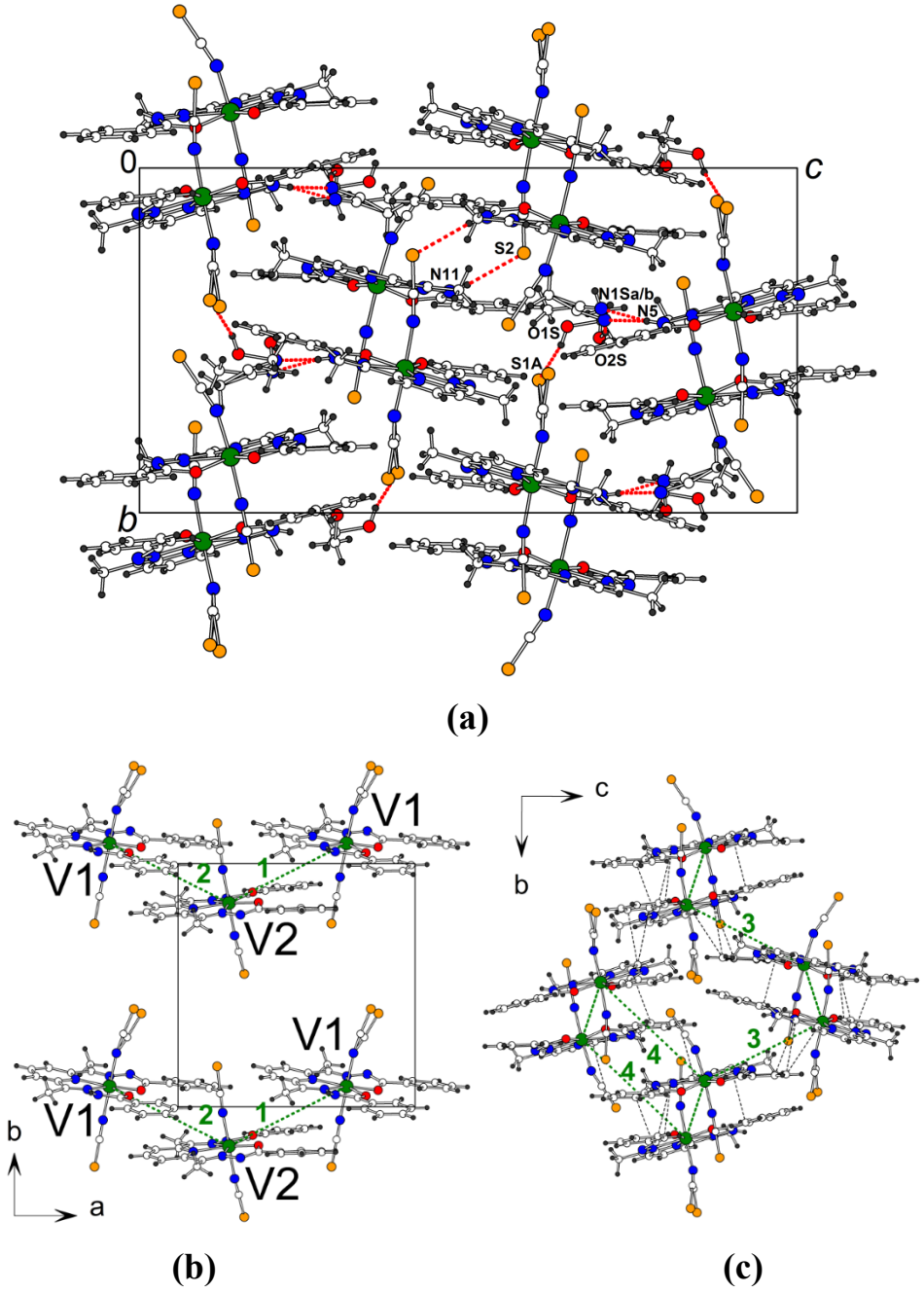

Figure S5. Projection of the structure **2** along *a*, chains look as dimers (a). View along *c*-direction to chains (b). View along *a*-direction to interchain interactions (c). Hydrogen bonds from acidic H-atoms (red dashed lines), C…C contacts < 3.6 Å (black dotted lines), V…V distances (green dashed lines, 1 = 7.8680(6), 2 = 7.9525(6), 3 = 8.1713(7), 4 = 8.8226(7) Å) are shown

Table S4. Hydrogen bond geometry in **2**.

D	H	A	Symmetry code for A	D-H, Å	H…A, Å	D…A, Å	D-H…A, º
N5	H5N	N1SA	x, y, z	0.82(4)	2.03(4)	2.829(10)	164(4)
N5	H5N	N1SB	x, y, z	0.82(4)	2.13(4)	2.944(9)	173(4)
N11	H11N	S2	x-0.5, 0.5-y, -z	0.83(3)	2.75(3)	3.563(2)	167(3)
O1S	H1S	S1A	1-x, y-0.5, 0.5-z	0.89(2)	2.36(2)	3.212(6)	160(2)
O2S	H2S	N1SB	x, y, z	0.85(3)	2.20(3)	3.020(15)	162(3)
C3	H3	S1A	x+0.5, 0.5-y, -z	0.95	2.89	3.683(3)	142.1
C3	H3	S1B	x+0.5, 0.5-y, -z	0.95	2.95	3.652(5)	132.0
C11	H11	S1A	x-0.5, 0.5-y, -z	0.95	2.90	3.690(3)	141.3
C16	H16C	N1SB	x, y, z	0.98	2.28	2.945(10)	123.9
C19	H19	N1SA	x, y, z	0.95	2.30	3.096(8)	141.1
C19	H19	N1SB	x, y, z	0.95	2.61	3.497(11)	156.2
C21	H21	S1A	2-x, y-0.5, 0.5-z	0.95	2.87	3.788(4)	163.1
C32	H32	S12	x+0.5, 1.5-y, -z	0.95	2.98	3.687(3)	132.7
C35	H35	S2	x-0.5, 0.5-y, -z	0.95	2.87	3.623(3)	137.6
C2SA	H2S2	S2	1-x, y+0.5, 0.5-z	0.98	2.55	3.34(3)	137.8
C2SA	H2S3	S12	1-x, y-0.5, 0.5-z	0.98	2.68	3.49(4)	139.9
C2SB	H2S2	S2	1-x, y+0.5, 0.5-z	0.98	2.38	3.06(3)	126.0
C2SB	H2S3	S12	1-x, y-0.5, 0.5-z	0.98	2.70	3.52(4)	141.2

[V(DAPBH)(MeOH)$_2$]Cl·MeOH (**3**)

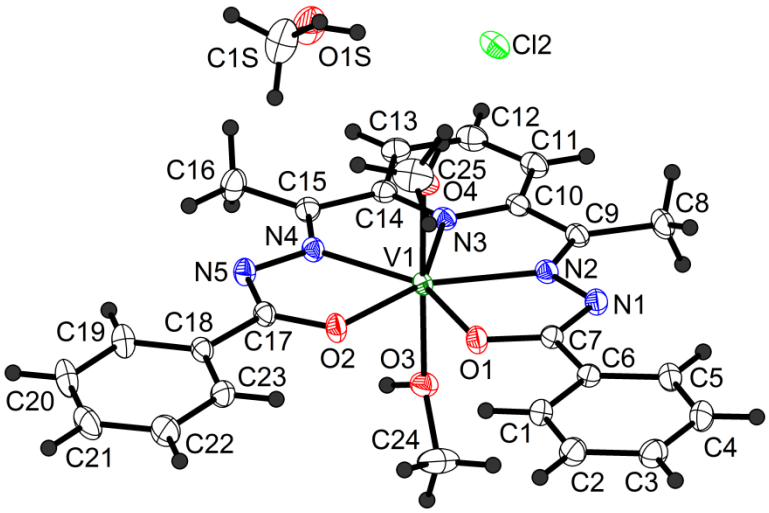

Figure S6. Asymmetric unit with atom numbering scheme in **3** (50% thermal ellipsoids).

Table S5. Selected bond lengths (Å) and angles (º) in **3**.

V1-O1	2.0109(8)	O1-C7	1.2889(13)	O2-C17	1.2892(14)
V1-O2	2.0193(8)	C7-N1	1.3212(14)	C17-N5	1.3147(15)
V1-N2	2.1524(9)	N1-N2	1.3831(14)	N5-N4	1.3835(13)
V1-N4	2.1473(10)	N2-C9	1.2980(14)	N4-C15	1.2943(15)
V1-N3	2.1424(9)	C9-C10	1.4597(16)	C15-C14	1.4648(15)
V1-O3	2.0901(9)	C10-N3	1.3494(14)	C14-N3	1.3491(15)
V1-O4	2.0629(9)				

O1-V1-N2	71.53(3)	O2-V1-N4	71.73(3)
O1-V1-N3	142.45(4)	O2-V1-N3	142.73(4)
O1-V1-N4	146.50(3)	O2-V1-N2	146.33(4)
N2-V1-N3	70.94(4)	N4-V1-N3	71.05(4)
O1-V1-O2	74.80(3)	N2-V1-N4	141.92(4)
O1-V1-O3	91.26(4)	O2-V1-O3	91.07(4)
N2-V1-O3	89.94(4)	N4-V1-O3	90.65(4)
O1-V1-O4	89.99(4)	O2-V1-O4	90.86(4)
N2-V1-O4	88.88(4)	N4-V1-O4	89.22(4)
N3-V1-O3	87.57(4)	N3-V1-O4	90.42(3)
O3-V1-O4	177.92(3)		

The V(III) complexes in **3** form layers parallel to the *ab* plane (Fig. S7). Average planes of $(DAPBH)^{2-}$ ligands are parallel within the layer but not parallel in adjacent layers along the *c*-axis (the corresponding dihedral angle between the VN_3O_2 planes is 54.03(2) º). In **3**, in the absence of NH proton, OH…Cl hydrogen bonds are formed between the axial methanol ligands and the Cl^- anions. Hydrogen bond geometry is given in Table S6. The nearest V…V distance in

the structure **3** is 7.498 Å along *b* in the infinite chains of the hydrogen-bonded V(III) complexes. The adjacent chains along *a* are paired through π-stacking of the ligands, the C…C distances less 3.6 Å are shown by black dotted lines in Fig. S7b, the V…V distance in this interaction is 8.655 Å.

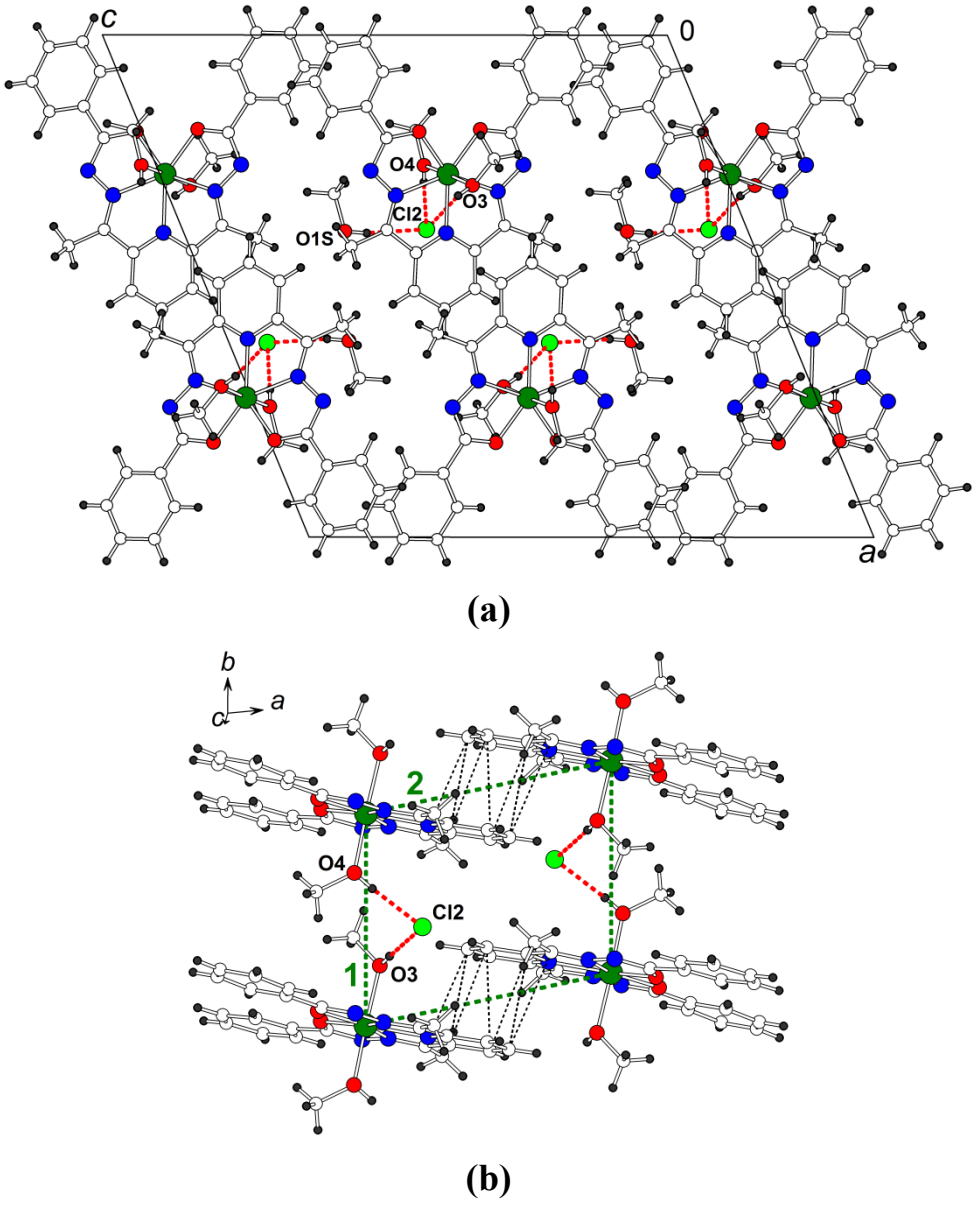

Figure S7. Projection of the structure **3** along *b* (a). The *ab* layer with hydrogen bonding and π-stacking interactions (b). Hydrogen bonds from acidic H-atoms (red dashed lines), C…C contacts < 3.6 Å (black dotted lines), V…V distances (green dashed lines, 1 = 7.4977(2), 2 = 8.6545(6) Å) are shown.

Table S6. Hydrogen bond geometry in **3**.

D	H	A	Symmetry code for A	D-H, Å	H…A, Å	D…A, Å	D-H…A, º
O3	H3A	Cl2	x, y+1, z	0.81(2)	2.19(2)	2.9935(10)	171(2)
O4	H4A	Cl2	x, y, z	0.81(2)	2.16(2)	2.9745(11)	176(2)
O1S	H1S	Cl2	x, y, z	0.84(3)	2.40(2)	3.2264(12)	170(2)
C11	H11	Cl2	1-x, 1-y, 1-z	0.95	2.71	3.6581(13)	173
C13	H13	O1S	1-x, y+0.5, 1.5-z	0.95	2.36	3.291(2)	166

Table S7. 1-3 complexes continuous Shape Measures calculations [1]

	Polyhedra						
Complex	HP	HPY	**PBPY**	COC	CTPR	JPBPY	JETPY
(**1**) $[V(H_2L)Cl_2]^+$	34.193	26.518	**0.481**	7.167	5.500	6.149	24.395
(**2**) $[V(HL)(NCS)_2]$ 1st center	33.416	25.258	**0.177**	7.097	5.199	3.444	23.076
(**2**) $[V(HL)(NCS)_2]$ 2nd center	34.077	25.175	**0.188**	7.056	5.234	3.319	23.489
(**3**) $[V(L)(MeOH)_2]^+$	34.491	25.942	**0.048**	8.095	6.227	3.519	24.835

HP – Heptagon (D_{7h}), HPY – Hexagonal pyramid (C_{6v}), **PBPY – Pentagonal bipyramid (D_{5h})**, COC – Capped octahedron (C_{3v}), CTPR – Capped trigonal prism (C_{2v}), JPBPY – Johnson pentagonal bipyramid (D_{5h}), JETPY – Johnson elongated triangular pyramid (C_{3v}).

1-3 complexes DFT optimized structures

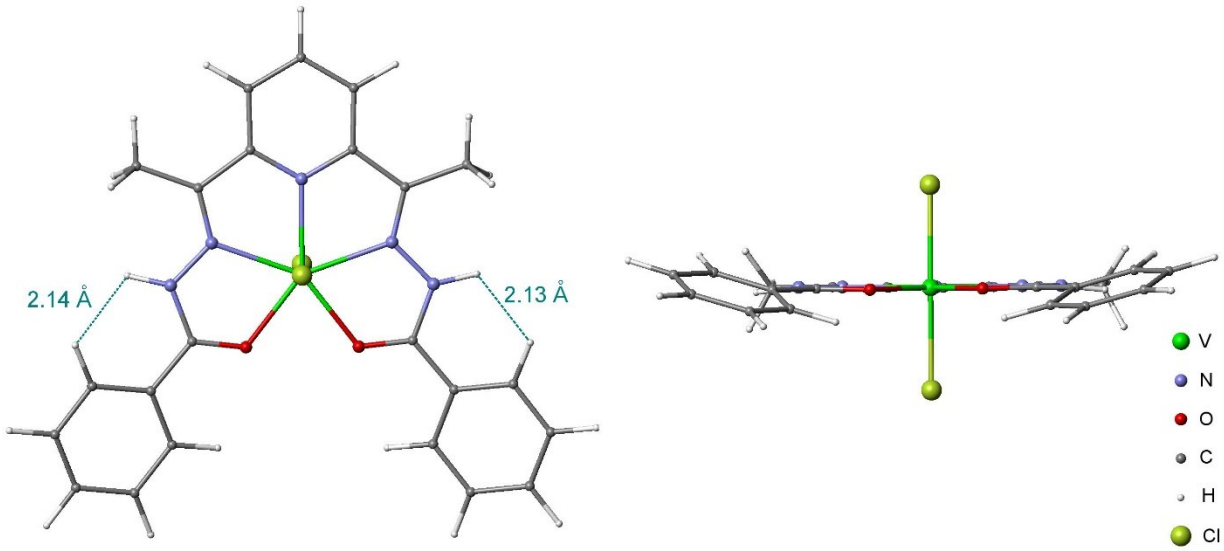

Figure S8. DFT optimized structure of complex $[V(H_2DAPBH)Cl_2]^+$ (**1**). Two phenyl rings rotate due to steric repulsion of two H atoms (separated by 2.14 Å and 2.13 Å, respectively, shown in dotted green line).

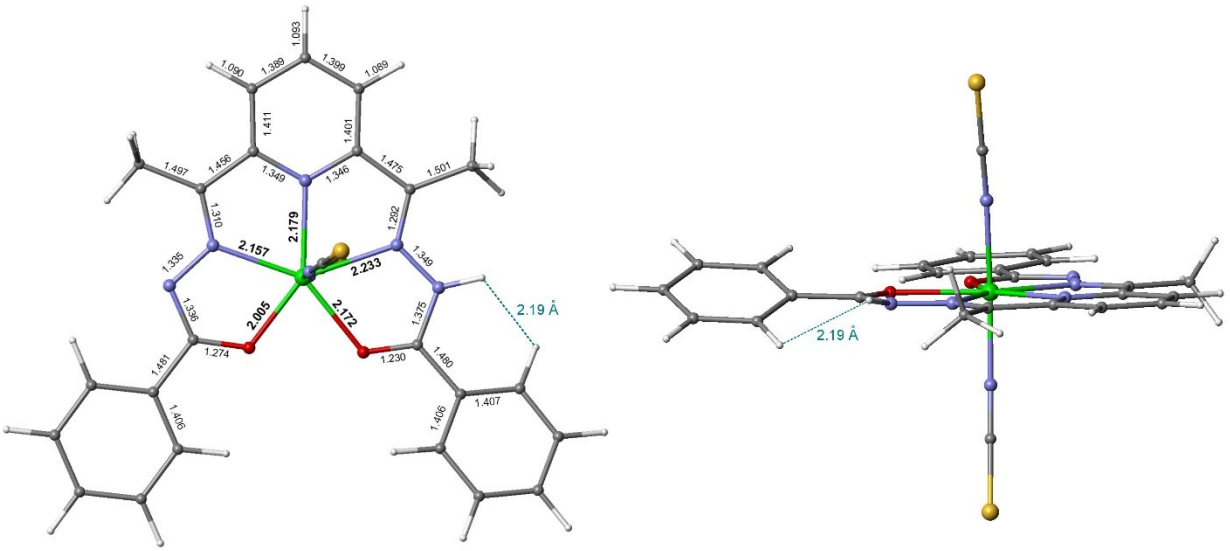

Figure S9. DFT optimized structure of $[V(HDAPBH)(NCS)_2]$ complex (**2**). The phenyl ring near to the protonated N atom rotates due to steric repulsion of two H atoms separated by 2.19 Å (shown in dotted green line). The second phenyl ring (near to the deprotonated N atom) is coplanar with the N_3O_2 plane due to the absence of close H…H contacts.

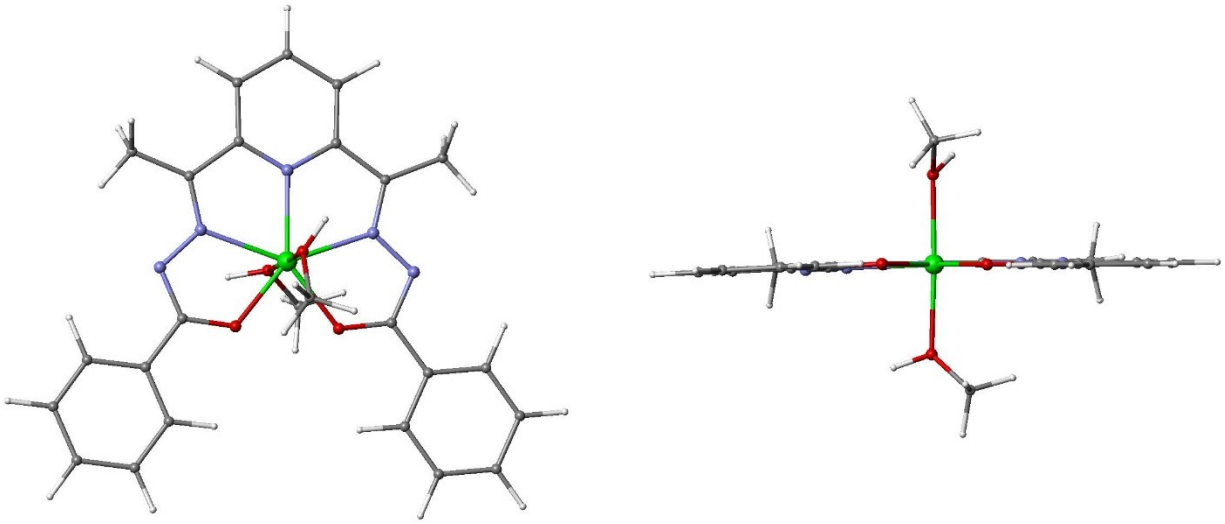

Figure S10. DFT optimized structure of complex $[V(DAPBH)(MeOH)_2]^+$ (**3**). The doubly deprotonated ligand DAPBH is planar due to the absence of close H…H contacts occurring in complexes **1** and **2** (Figs. S8 and S9).

HF-EPR studies

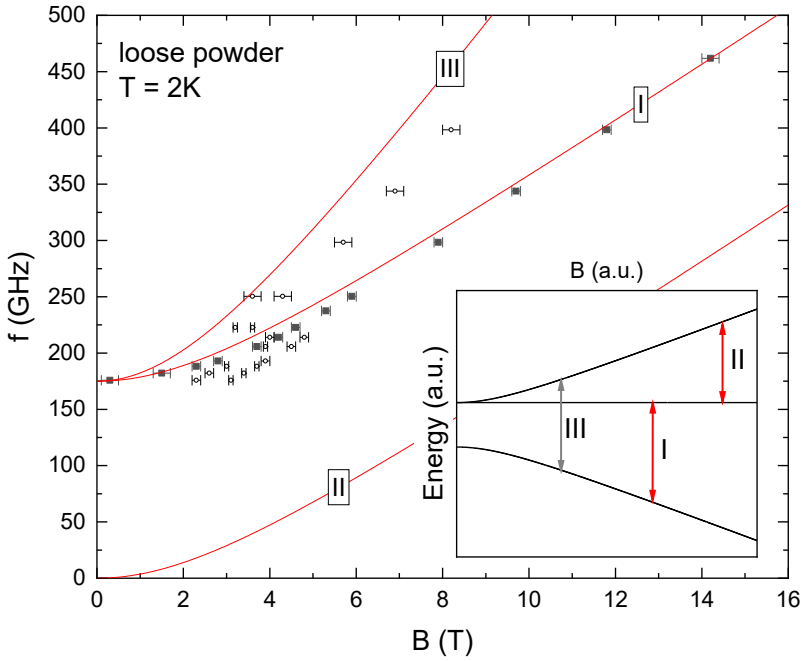

Figure S11. Magnetic field dependence of the resonance frequencies for a loose powder sample of **3**, at T = 2 K (Fig. 8 shows data obtained at higher temperatures, too). Filled squares correspond to the main feature while open circles show features which are only slightly visible and arising from forbidden or excited transitions (cf. Fig. 6, 7). Simulation of resonance branches by means of a monomeric $S = 1$ model (i.e., without considering intermolecular coupling) fails. A best simulation using monomeric SH with $D = 175$ GHz and $g = 1.83$ is shown by red lines. Inset: Corresponding arbitrary energy level diagram with allowed (red arrows) and forbidden (grey arrow) transitions.

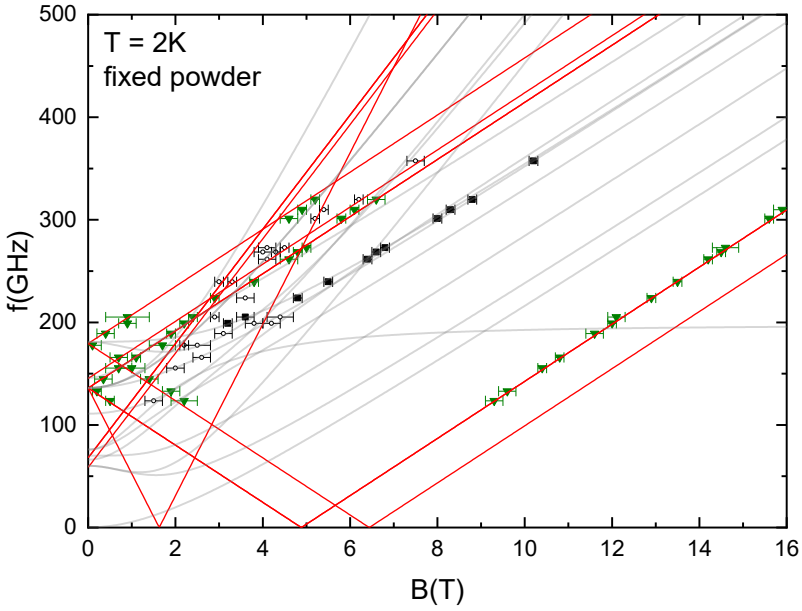

Figure S12. Magnetic field dependence of the resonance frequencies for a fixed powder sample of **3**, at T = 2 K. Green triangles show features which were absent in the loose powder measurements and can be attributed to features arising from the axial direction of the molecular frame. The black squares show the resonance branch which was already obtained in the loose powder measurement. Red lines show a simulation of the parallel branches ($\boldsymbol{B}_{ext} \parallel g_{\parallel}$) while the grey lines reproduce a simulation of $\boldsymbol{B}_{ext} \parallel g_{\perp}$. Open circles show features with much less intensity as compared to the main branch which can be attributed to excited or forbidden transitions.

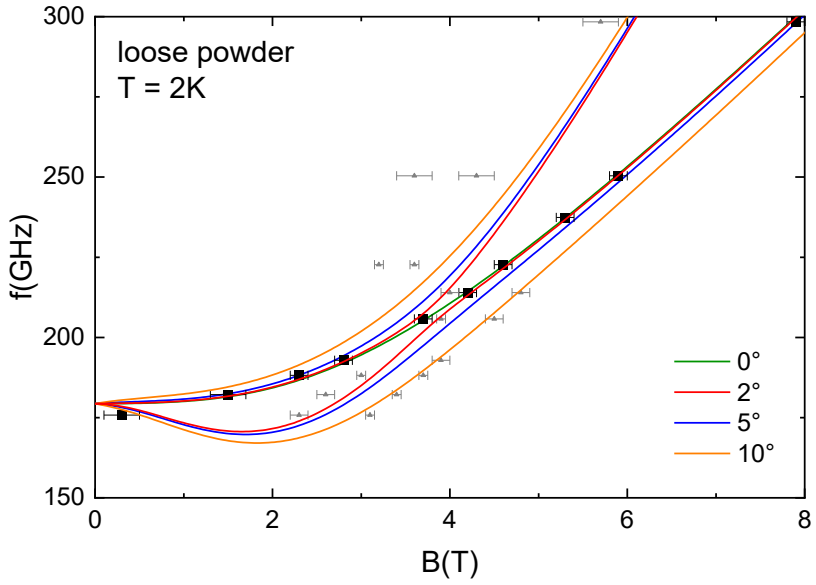

Figure S13. Magnetic field dependence of the resonance frequencies for a loose powder sample of **3**, at T = 2 K, and respective simulation results. Filled squares correspond to the main feature while grey symbols show features which are only slightly visible and associated with forbidden or excited transitions (cf. Fig. 6, 7). The solid lines visualize simulations of the observed main branch which corresponds to the ground state transition using the SH for a coupled dimer system shown in Eqn. 2 with the parameters listed in Tab. 4 and different angles between the direction of the crystal field xy-plane and the external magnetic field.

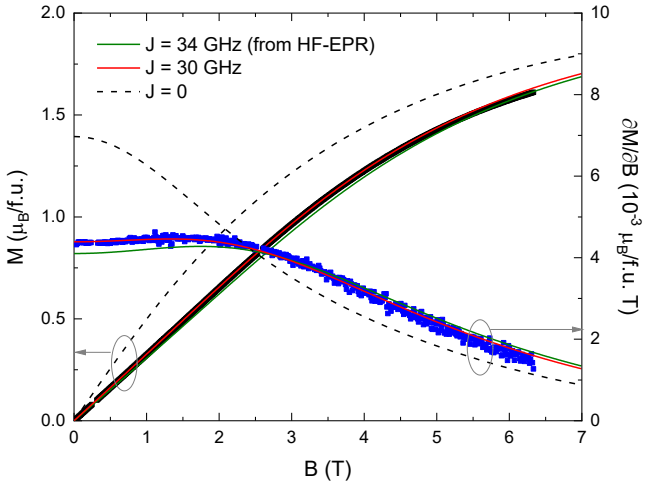

Figure S14. DC magnetization of (3) vs. magnetic field (black symbols,; left ordinate) and its derivative (blue symbols; right ordinate) obtained at T = 2 K. Solid lines show simulations using the dimer model SH in Eqn. 2 with a coupling constant of J = 34 GHz (green) and J = 30 GHz (red), respectively. The dashed lines correspond to a simulation using a monomeric model for the vanadium centers.

Ligand-field calculations for the [V^{III}(H_nDAPBH)X_2] complexes.

LF calculations for [V^{III}(H_nDAPBH)X_2]$^{+m}$ complexes **1-3** are performed in terms of a conventional model LF Hamiltonian

$$H_{\mathrm{LF}} = \sum_{i>j} \frac{e^2}{|\boldsymbol{r}_i - \boldsymbol{r}_j|} + \zeta_{3d} \sum_i \boldsymbol{l}_i \boldsymbol{s}_i + V_{\mathrm{LF}} + \mu_B (k\boldsymbol{L} + 2\boldsymbol{S})\boldsymbol{H}\,, \qquad (\mathrm{S1})$$

where the first term represents Coulomb repulsion between 3*d* electron of (where *i* and *j* runs over 3*d* electrons), the second term is the spin-orbit coupling (*SOC)* of V centers, V_{LF} is a ligand-field Hamiltonian, and the last term refers to the Zeeman interaction with the external magnetic field ***H***. In these calculations, the B = 632 and C =2877cm^{-1} Racah parameters for the Coulomb term in (S1), the SOC constant ζ_{3d} = 165 cm^{-1} and the k = 0.8 orbital reduction factor in the Zeeman term.[2] The matrix elements of the LF operator V_{LF} is calculated in terms of the angular overlap model (AOM).[3] For [V^{III}(H_nDAPBH)X_2] complexes **1-3** the AOM parameters e_σ = 6100 cm^{-1} and e_σ/e_π = 0.144 are employed for all the N and O coordinating atoms involved in the pentagonal N_3O_2 ring of DAPBH ligand and two apical X atoms (see Figs. S2, S4 and S6); the radial dependence of the AOM parameters is approximated by $e_{\sigma,\pi}(R) = e_{\sigma,\pi}(R_0)(R_0/R)^n$ with n=4 and R_0 = 2.09 Å. For the apical Cl ligands in **1** the e_σ = 9000 cm^{-1} and e_σ/e_π = 0.25 were used (at R_0 = 2.35 Å). The actual geometry of [V^{III}(H_nDAPBH)X_2] complexes is employed. The energy levels of $3d^2$ are obtained by a numerical diagonalization of (S1) in the full set of $3d^2$ many electron wave functions involving 45 $|LM_LSM_S\rangle$ microstates. Calculated orbital splitting

energies are shown in Table S8, the energies of $3d^2$ LF states are listed in Table S9. Calculated energies of low-lying spin-orbit states $E_n(j)$ of $[V^{III}(H_nDAPBH)X_2]$ complexes **1-3** are given in Table S10. The three lowest spin-orbit states $E_n(j)$ refer to the ZFS energies are described by the S=1 *ZFS* spin Hamiltonian $DS_z^2 + E(S_x^2 - S_y^2)$ with D and E parameters listed in Table S10.

Table S8. Calculated LF energy levels (cm^{-1}) of 3d orbitals in compounds **1-3**.

Compound		
1	**2**	**3**
Energy of 3d orbitals, cm^{-1}		
0	0	0
36	146	101
7719	80476	8491
9573	10573	10957
19914	16503	16258

Table S9. Calculated energies of $3d^2$ LF states of V(III) in compounds **1-3**. Triplet states are marked in blue.

Compound		
1	**2**	**3**
Energy of $3d^2$ LF states, cm^{-1}		
0	0	0
7025	7358	7736
7098	7393	7816
9916	9935	9909
9983	9953	9928
9994	10142	10538
10034	10581	10721
15037	15213	15318
16539	16833	17266
16578	17015	17353
20860	21596	22003
20883	21645	22017
24087	22435	22453

25255	22490	22746
25735	23582	23378
26917	25434	25632
28179	25648	26310
28964	27887	27727
29294	28216	27925

Table S10. Calculated energy levels of three lowest spin-orbit states and ZFS parameters *D* and *E* of the ground triplet state of compounds **1**-**3**.

Compound		
1	**2**	**3**
Energy of spin-orbit states, cm^{-1}		
0	0	0
3.87	3.91	3.92
3.94	4.09	4.04
ZFS parameters, cm^{-1}		
$D = 3.91$	$D = 4.00$	$D = 3.98$
$E = 0.035$	$E = 0.09$	$E = 0.06$

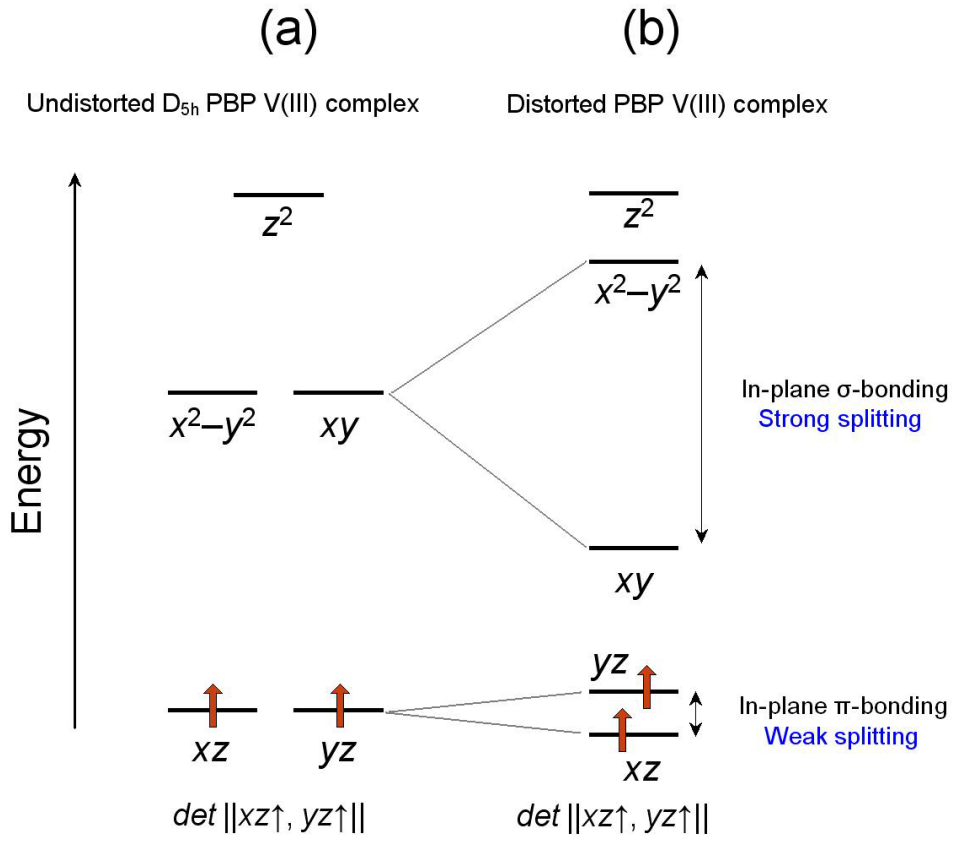

The two-electron wave function *det* ||*xz*↑, *yz*↑|| of the ground-state is insensitive to in-plane distortions.

- High-spin ground state $S = 1$
- Zero orbital momentum (the spin-only case)
- Second-order ZFS magnetic anisotropy with $D > 0$
- Weak in-plane magnetic anisotropy ($E << D$)

Figure S15. Energy splitting of 3d orbitals in (a) undistorted (D_{5h}) and (b) distorted PBP V(III) complexes and the orbital composition of the two-electron ground-state wave function *det*||*xz*↑, *yz*↑||. Small energy splitting of $3d_{xz}$ and $3d_{yz}$ orbitals leads to the fact that the ground-state wave function *det*||*xz*↑, *yz*↑|| is insensitive to the in-plain distortions in PBP V(III) complexes **1**-**3**.

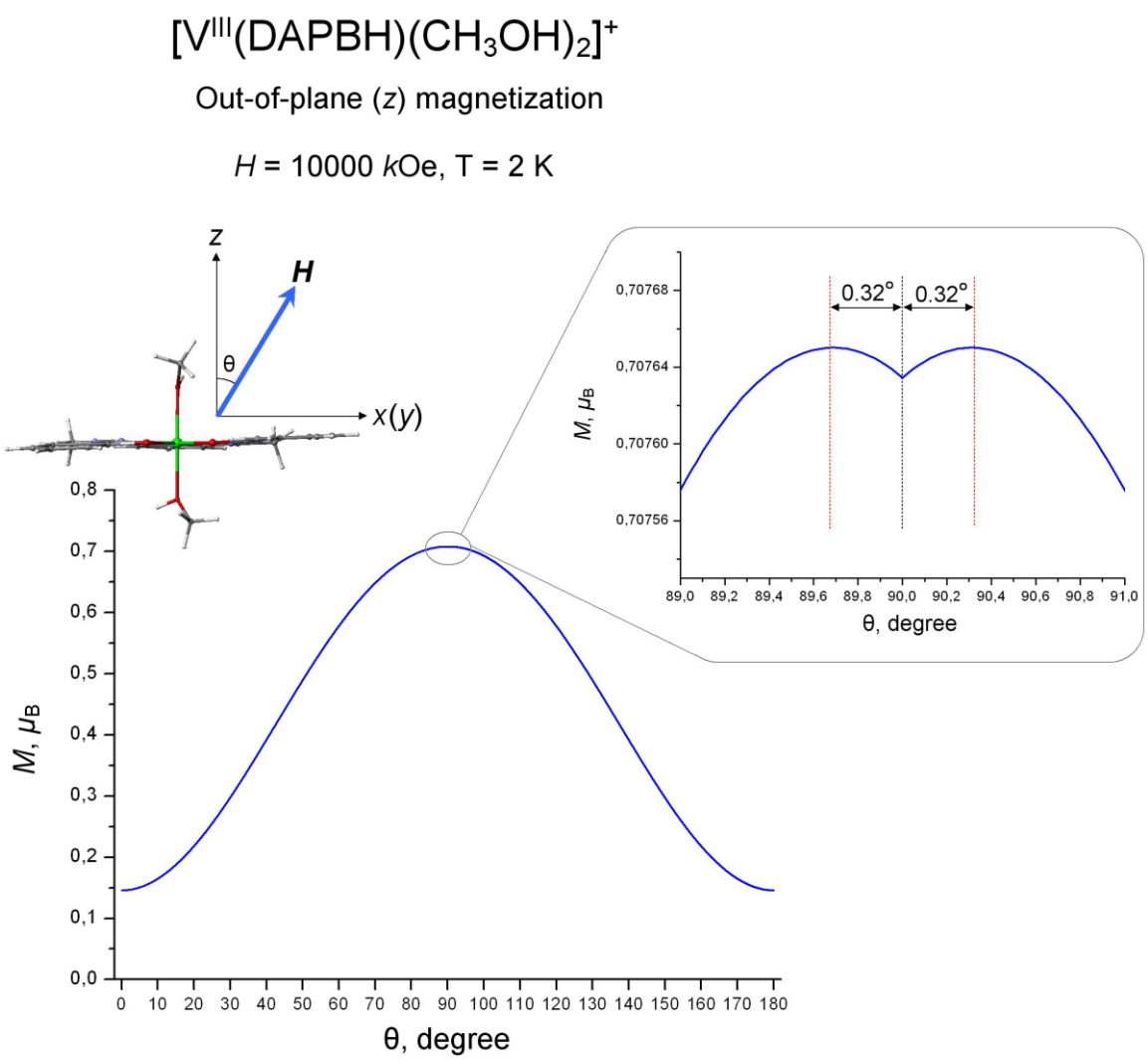

Figure S16. Calculated angular variation of the out-of-plane magnetization $M(\theta)$ of complex $[V^{III}(DAPBH)(CH_3OH)_2]^+$ in **3** (at H = 10000 kOe and T = 2 K). Complex displays strongly positive magnetic anisotropy with a distinct maximum of magnetization in the equatorial VN_3O_2 plane (xy), with a deviation from it within ~ 0.3° (shown in the inset). Calculations are performed with Eq. S1 using atomic and AOM parameres listed above in the Section.

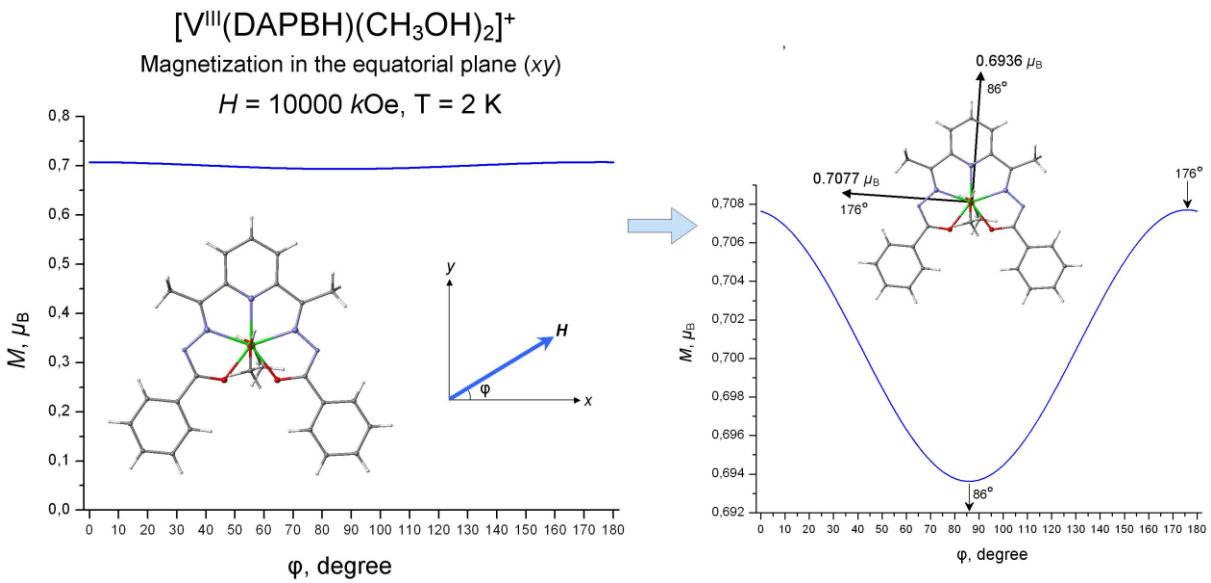

Figure S17. Calculated angular variation of the in-plane magnetization $M(\varphi)$ of complex $[V^{III}(DAPBH)(CH_3OH)_2]^+$ in **3** (at H = 10000 kOe and T = 2 K). In the equatorial plane (***H*** || *xy*), magnetization is nearly isotropic with respect to the azimuthal angle φ. On the right: the orientations of the two principal magnetic axes in the equatorial VN_3O_2 plane *xy* are indicated. These two in-plane principal axes are almost equivalent in the magnetization. Calculations are performed with Eq. S1 using atomic and AOM parameres listed above in the Section.

Microscopic calculations of exchange parameters for V(III) – V(III) pairs in terms of the many-electron superexchange theory.

This section describes details of microscopic calculations of the exchange parameters J in V(III) pairs in compound **3**. Calculations are performed in terms of a many-electron superexchange model, which has been first presented in ref.[4] and then further developed in.[5]

At the first step, many-electron wave functions $\Phi_k(\mathrm{A}, 3\mathrm{d}^N)$, $\Phi_l(\mathrm{B}, 3d^M)$ and their energies $E_k(\mathrm{A}, 3\mathrm{d}^N)$, $E_l(\mathrm{B}, 3d^M)$ are calculated for the V^{III}(A) and V^{III}(B) magnetic centers in the basic electronic configurations ($3d^2$(A) and $3d^2$(B)) and in charge-transfer (*CT*) configurations resulting from migration of one electron between V^{III}(A) and V^{III}(B), $3d^2$(A)+ $3d^2$(B) → $3d^1$(A)+ $3d^3$(B) and $3d^2$(A)+ $3d^2$(B) → $3d^3$(A)+ $3d^1$(B). These wave functions are eigenvectors of the one-center ligand-field (*LF*) Hamiltonians H_A and H_B for the magnetic centers V^{III}(A) and V^{III}(B) (see Fig. S19) with neglected spin-orbit coupling

$$H_{\mathrm{A,B}} = \sum_{i>j} \frac{e^2}{|\boldsymbol{r}_i - \boldsymbol{r}_j|} + \quad V_{LF}\,, \qquad (\mathrm{S2})$$

where the first term represents Coulomb repulsion between 3*d* electrons and V_LF is a ligand-field Hamiltonian for V(A) and V(B) centers,

$$H_\mathrm{A}\Phi_k(\mathrm{A}, 3d^2) = E_k(\mathrm{A}, 3d^2)\,\Phi_k(\mathrm{A}, 3d^2), \qquad (\mathrm{S3})$$

$$H_\mathrm{B}\Phi_l(\mathrm{B}, 3d^2) = E_l(\mathrm{B}, 3d^2)\,\Phi_l(\mathrm{B}, 3d^2)\,, \qquad (\mathrm{S4})$$

$$H_\mathrm{A}\Phi_p(\mathrm{A}, 3d^1) = E_p(\mathrm{A}, 3d^1)\,\Phi_p(\mathrm{A}, 3d^1), \qquad (\mathrm{S5})$$

$$H_\mathrm{B}\Phi_q(\mathrm{B}, 3d^1) = E_q(\mathrm{B}, 3d^1)\,\Phi_q(\mathrm{B}, 3d^1), \qquad (\mathrm{S6})$$

$$H_\mathrm{A}\Phi_r(\mathrm{A}, 3d^3) = E_r(\mathrm{A}, 3d^3)\,\Phi_r(\mathrm{A}, 3d^3), \qquad (\mathrm{S7})$$

$$H_\mathrm{B}\Phi_s(\mathrm{B}, 3d^3) = E_s(\mathrm{B}, 3d^3)\,\Phi_s(\mathrm{B}, 3d^3), \qquad (\mathrm{S8})$$

where the spin variables ($S_\mathrm{A}M_S$ and $S_\mathrm{B}M_S$) are omitted for brevity. Then pair-ion many-electron wave functions of the V^{III}(A)-V^{III}(B) pair are constructed from the single-ion many-electron wave functions (S3-S8):

$$\Psi_{kl}(\mathrm{AB}) = \Phi_k(\mathrm{A}, 3d^2)\times\Phi_l(\mathrm{B}, 3d^2), \qquad (\mathrm{S9})$$

$$\Xi_{pq}(\mathrm{A}\rightarrow\mathrm{B}) = \Phi_p(\mathrm{A}, 3d^1)\times\Phi_q(\mathrm{B}, 3d^3), \qquad (\mathrm{S10})$$

$$\Xi_{rs}(\mathrm{A}\leftarrow\mathrm{B}) = \Phi_r(\mathrm{A}, 4d^3)\times\Phi_s(\mathrm{B}, 3d^1), \qquad (\mathrm{S11})$$

where × stands for the antisymmetrized product. Due to neglected spin-orbit coupling on the V(A) and V(B) centers, all pair-ion states (S9-S11) have a definite total spin S (ranging from $|S_A–S_B|$ to S_A+S_B) and its projection M_S. The spin-adapted wave functions $\Psi_{kl}(AB; SM_S)$, $\Xi_{pq}(A\rightarrow B; SM_S)$ and $\Xi_{rs}(A\leftarrow B; SM_S)$ with definite S and M_S are obtained from wave functions (S9-S11) using the conventional spin projection technique.

At the second step, matrix elements of the effective spin Hamiltonian $H_{eff} = A – \boldsymbol{JS}_A\boldsymbol{S}_B$ are obtained by projection of the *CT* states $\Xi_{pq}(A\rightarrow B; SM_S)$ and $\Xi_{rs}(A\leftarrow B; SM_S)$ onto the space of the ground-state wave functions $\Psi(AB; SM_S) = \Psi_{11}(AB; SM_S)$ (where indexes k=1 and l=1 for the ground state are omitted) in the second-order perturbation theory,

$$\left\langle \Psi\,(\mathrm{AB};SM_S)\middle|H_{\mathrm{eff}}\middle|\Psi\,(\mathrm{AB};SM_S)\right\rangle =$$
$$-\sum_{pq}\frac{\left\langle \Psi\,(\mathrm{AB};SM_S)\middle|H\middle|\Xi_{pq}(\mathrm{A}\rightarrow\mathrm{B};SM_S)\right\rangle\left\langle \Xi_{pq}(\mathrm{A}\rightarrow\mathrm{B};SM_S)\middle|H\middle|\Psi\,(\mathrm{AB};SM_S)\right\rangle}{E_{pq}(\mathrm{A}\rightarrow\mathrm{B})}$$
$$-\sum_{rs}\frac{\left\langle \Psi\,(\mathrm{AB};SM_S)\middle|H\middle|\Xi_{rs}(\mathrm{A}\leftarrow\mathrm{B};SM_S)\right\rangle\left\langle \Xi_{rs}(\mathrm{A}\leftarrow\mathrm{B};SM_S)\middle|H\middle|\Psi\,(\mathrm{AB};SM_S)\right\rangle}{E_{rs}(\mathrm{A}\leftarrow\mathrm{B})}, \qquad (S12)$$

where H is a perturbation Hamiltonian

$$H=\sum_k h(k), \qquad (S13)$$

which is a sum of one-electron operators $h(k)$ (with index k running over $3d$(A) and $3d$(B) electrons of the V(A)-V(B) pair) describing one electron transfers between the V(A) and V(B) metal centers. The operator h is specified by the set of electron transfer parameters t_{ij}, which are one-electron matrix elements $t_{ij} = \langle 3d_i(A)|h|3d_j(B)\rangle$ connecting $3d_i$(A) and $3d_j$(B) magnetic orbitals centered on different metal sites A and B; i and j are orbital indexes, $i, j = xy, yz, zx, x^2–y^2$, and z^2. The energies $E_{pq}(A\rightarrow B)$ and $E_{rs}(A\leftarrow B)$ in (S12) are expressed by

$$E_{pq}(A\rightarrow B) = U_0(A\rightarrow B) + E_p(A, 3d^1) + E_q(B, 3d^3), \qquad (S14)$$
$$E_{rs}(A\leftarrow B) = U_0(A\leftarrow B) + E_r(A, 3d^3) + E_s(B, 3d^1), \qquad (S15)$$

where $U_0(A\rightarrow B)$ and $U_0(A\leftarrow B)$ are the charge-transfer energies. The spin dependence of each matrix element $\left\langle \Psi\,(\mathrm{AB};SM_S)\middle|H_{eff}\middle|\Psi\,(\mathrm{AB};SM_S)\right\rangle$ in (S12) obeys the Lande pattern; therefore, the set of the matrix elements (S12) exactly corresponds to an effective spin Hamiltonian

$$H_{\mathrm{eff}} = A – \boldsymbol{JS}_A\boldsymbol{S}_B, \qquad (S16)$$

where A and J are spin-independent and spin-dependent exchange parameters. Then, A and J are obtained from equating matrix elements $\langle\Psi(AB; SM_s)|\ A–\boldsymbol{JS}_A\boldsymbol{S}_B\ |\Psi(AB; SM_s)\rangle$ to the matrix

elements of (S12). This superexchange model is implemented by a computer code, which has been applied to evaluate the *A* and *J* exchange parameters for in compound **3**.

Superexchange calculations are performed for various vanadium pairs in compound **3** depicted below in Figs. S18-S20.

The $V^{III}(A)\rightarrow V^{III}(B)$ and $V^{III}(A)\leftarrow V^{III}(B)$ charge-transfer energies are set to $U_0(A\rightarrow B) = U_0(A\leftarrow B) = 40000$ cm^{-1} (5 eV). In the Coulomb term of the LF Hamiltonians H_A and H_B (S1), the $B = 632$ and $C = 2877$ cm^{-1} Racah parameters are used for V^{III} ions.[2] Considering high axial symmetry of [V(DAPBH)$(CH_3OH)_2$] complexes, for V^{III}-centers the LF operator V_{LF} is applied in the diagonal form specified by the set of one-electron orbital energies for a pentagonal-bipyramidal ligand coordination, 0 ($3d_{xz}$, $3d_{yz}$), 9000 cm^{-1} ($3d_{xy}$, $3d_{x2-y2}$) and 16000 cm^{-1} ($3d_{z2}$), corresponding to average orbital energies obtained from AOM calculations (see Table S8 for complex **3**).

The set of one-electron matrix elements $t_{ij} = \langle 3d_i(A)|h|3d_j(B)\rangle$ is obtained from extended Hückel (*EH*) calculations (with standard atomic parameterization)[6] for the actual crystallographic structure of the V^{III}–V^{III} exchange-coupled pairs 1 and 2 in compound **3** (Fig. S19) following the computational scheme described in ref.[7] , according to which ten 3*d*-rich molecular orbitals of the V^{III}– V^{III} pair are projected onto pure 3*d*(A) and 3*d*(B) atomic orbitals of two metal atoms. Specifically, starting from EH molecular orbitals ψ_n

$$H_{EH}\psi_n = E_n\psi_n\,, \qquad (S16)$$

the projected $\boldsymbol{P}\psi_n$ atomic orbitals on the metal centers V(A) and V(B) are specified as eigenvectors of an efficient electron transfer Hamiltonian H'_{eff}

$$H'_{eff}\,\boldsymbol{P}\psi_n = E_n\,\boldsymbol{P}\psi_n, \qquad (S17)$$

Importantly, H'_{eff} is a non-Hermitian operator; it transforms to a Hermitian operator $H'^{(H)}_{eff}$ by

$$H'^{(H)}_{eff} = (H'_{eff} + H'^{T}_{eff})/2. \qquad (S18)$$

In the space of ten $3d_i$(A) and $3d_j$(B) atomic orbitals $H'^{(H)}_{eff}$ is written as a 10×10 symmetric matrix. Its off-diagonal 5×5 block (non-symmetric) corresponds to the set of electron transfer parameters $t_{ij} = \langle 3d_i(A)|h|3d_j(B)\rangle$ connecting magnetic orbitals of V(A) and V(B), which specify the perturbation kinetic Hamiltonian *H* involved in (S12) and (S13). Calculated electron transfer parameters $t_{ij} = \langle 3d_i(A)|h|3d_j(B)\rangle$ (in cm^{-1}) for the two V^{III}(A)–V^{III}(B) pairs exchange-coupled pairs (Fig. S19a,b) are given by the following 5×5 matrices,

$$\begin{pmatrix} A\downarrow B\rightarrow & x^2-y^2 & xy & z^2 & xz & yz \\ x^2-y^2 & -0.8 & -0.1 & 2.3 & -1.7 & -3.5 \\ xy & -0.6 & -0.9 & -5.6 & -0.6 & -1.2 \\ z^2 & 3.2 & 4.0 & 9.4 & 42.4 & 1.1 \\ xz & -1.2 & -1.5 & -38.5 & -1.7 & 2.0 \\ yz & 1.6 & -2.6 & 2.4 & 2.4 & 10.7 \end{pmatrix} \quad (S19)$$

for the pair 1 (Fig. S19a) and,

$$\begin{pmatrix} A\downarrow B\rightarrow & x^2-y^2 & xy & z^2 & xz & yz \\ x^2-y^2 & -1.9 & 4.3 & 0.0 & 7.7 & -10.8 \\ xy & 4.4 & -1.4 & -4.0 & 2.3 & 0.7 \\ z^2 & -0.1 & -4.2 & -4.7 & -10.8 & -99.2 \\ xz & 9.2 & 3.0 & -5.6 & 136.5 & 58.2 \\ yz & -10.9 & 1.0 & -94.2 & 61.6 & 5.9 \end{pmatrix} \quad (S20)$$

for the pair 2 (Fig. S19b). With these sets of parameters, superexchange calculations using Eq. (S12) result in the effective exchange spin Hamiltonian $H_{\text{eff}} = A - J\boldsymbol{S}_{\text{A}}\boldsymbol{S}_{\text{B}}$ with spin-independent and spin dependent parameters $A = -0.06$, $J = +8.4\cdot10^{-4}$ cm^{-1} for pair 1 (Fig. S19a) and $A = -0.86$, $J = -0.49$ cm^{-1} for pair 2 (Fig. S19b).

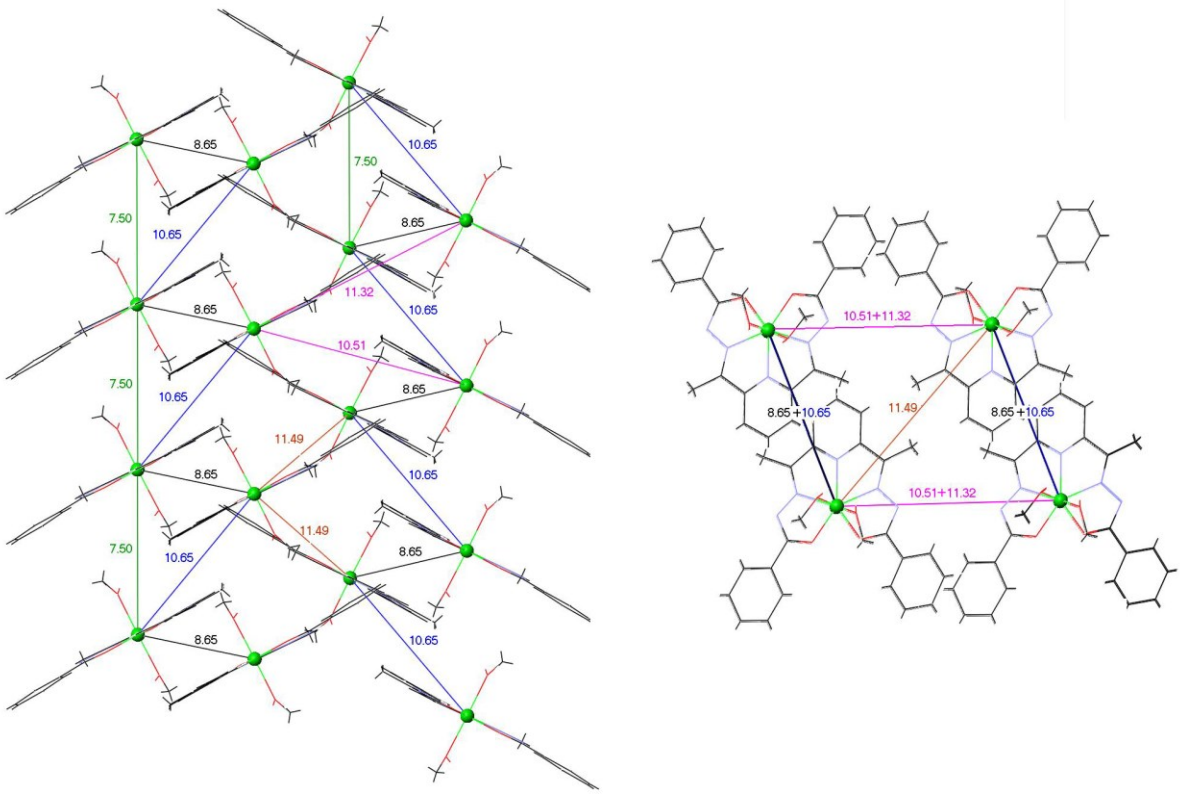

Figure S18. Zig-zag chains in the crystal structure of **3**. Chains are formed by two vanadium pairs with short (8.65 Å) and long (10.65 Å) V…V distances, in which $[V^{III}(DAPBH)(CH_3OH)_2]^+$ complexes are connected via the π-π stacking contacts of macrocyclic rings (two projections are shown).

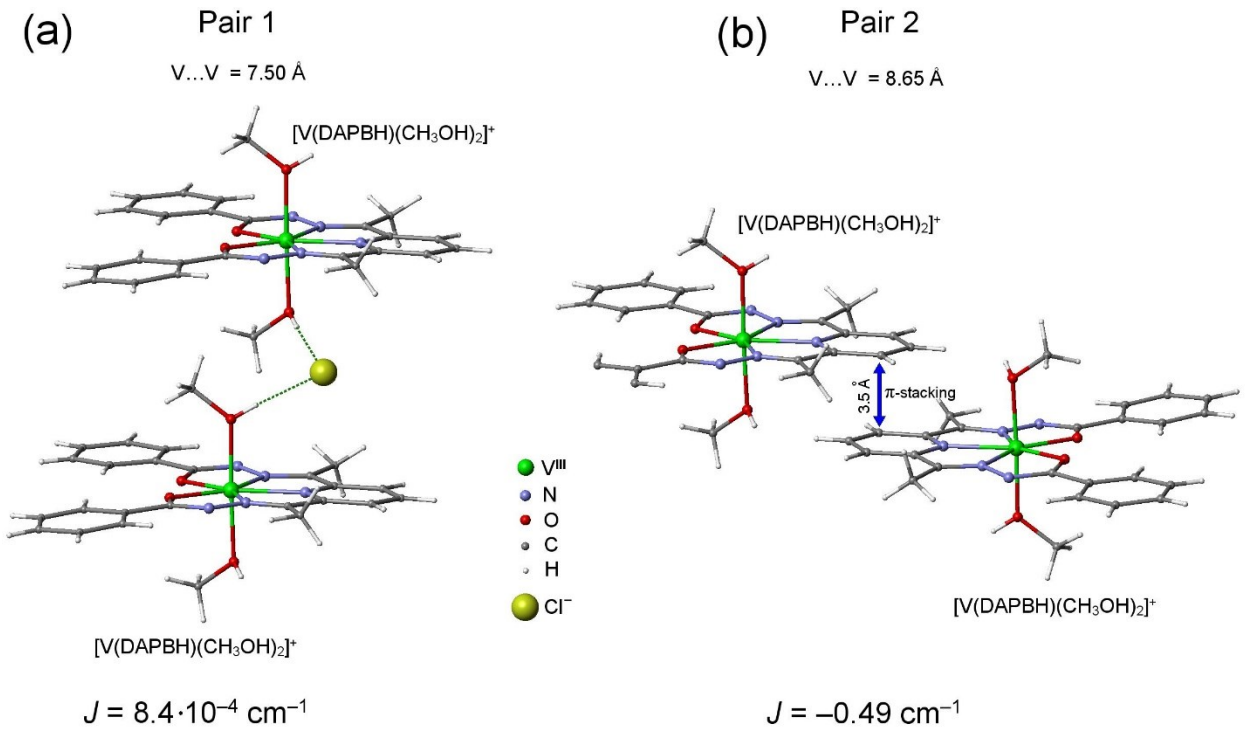

Figure S19. Calculated exchange parameters J for the two V(III)-V(III) pairs 1 and 2 in compound **3** composed of two closest units $[V(DAPBH)(CH_3OH)_2]^+$ contacting (a) via hydrogen bonding (shown in dotted green lines) involving Cl^- anion (pair 1, $J = 8.4{\cdot}10^{-4}$ cm^{-1}) and (b) via π-stacking of two planar DAPBH ligands separated by ~3.5 Å (pair 2, pronounced AF spin coupling of $J = -0.49$ cm^{-1}).

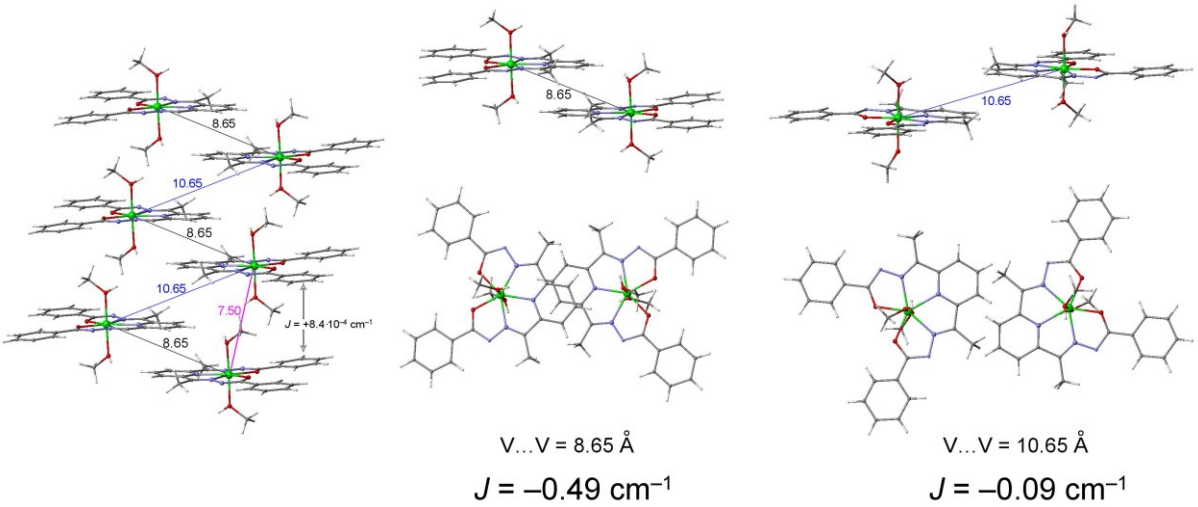

Figure S20. Structure of the short (V…V = 8.65 Å) and long (V…V = 10.65 Å) vanadium pairs in the zig-zag chains in the crystal structure of **3**. In both pairs the $[V^{III}(DAPBH)(CH_3OH)_2]^+$ units contacts via the π-π stacking of macrocyclic aromatic rings. In the short pair these rings overlap considerably better than in the long pair (as shown in the apical projection in the bottom) thereby resulting in better performance of the π-π stacking as mediator of the long-range spin coupling between V(III) ions, $J = -0.49$ cm^{-1} (8.65 Å) vs. $J = -0.09$ cm^{-1} (10.65 Å).

Modeling of the spin energy spectra V(III)-V(III) exchange-coupled pairs, magnetization and magnetic susceptibility of complex 3 in terms of the dimer-like model.

Energy spectra of spin states and magnetic susceptibility of V(III)-V(III) exchange-coupled pairs in **3** (Fig. S19) are calculated in terms of a spin Hamiltonian

$$H = -J\boldsymbol{S}_1\boldsymbol{S}_2 + \sum_{k=1,2} D(S_k^z)^2 + \mu_B g\boldsymbol{H}\sum_{k=1,2}\boldsymbol{S}_k \,, \qquad (S21)$$

where index k runs over two V^{III} magnetic centers involved in the pairs (Fig. S19). The components M_α ($\alpha = x, y, z$) of the magnetic moment $\boldsymbol{M}$ of vanadium complexes in an external magnetic field $\boldsymbol{H}$ are obtained from the conventional equation

$$M_\alpha = Nk_BT\frac{\partial \ln Z(\boldsymbol{H})}{\partial H_\alpha}, \qquad (S22)$$

where $Z(\boldsymbol{H})$ is the partition function

$$Z(\boldsymbol{H}) = \sum_i \exp(-E_i(\boldsymbol{H})/k_BT), \qquad (S23)$$

with $E_i(\boldsymbol{H})$ being the energy of the i-th electronic state of the cluster in the magnetic field $\boldsymbol{H}$ obtained from diagonalization of the spin Hamiltonian (S21). Then the diagonal component $\chi_{\alpha\alpha}$ of the tensor of magnetic susceptibility is written as $\chi_{\alpha\alpha} = M_\alpha / H_\alpha$; magnetic susceptibility of the powder sample is given by $\chi = (\chi_{xx} + \chi_{yy} + \chi_{zz})/3$. Calculations of magnetic susceptibility are performed at the experimental applied magnetic field of H = 1 kOe. With this approach, the temperature dependence of magnetic susceptibility was calculated (Fig. 5a-c, main text); the simulated χT product of compound **3** is shown in Fig. S21 and compared with the χT product obtained with single-ions model (Fig. 5c).

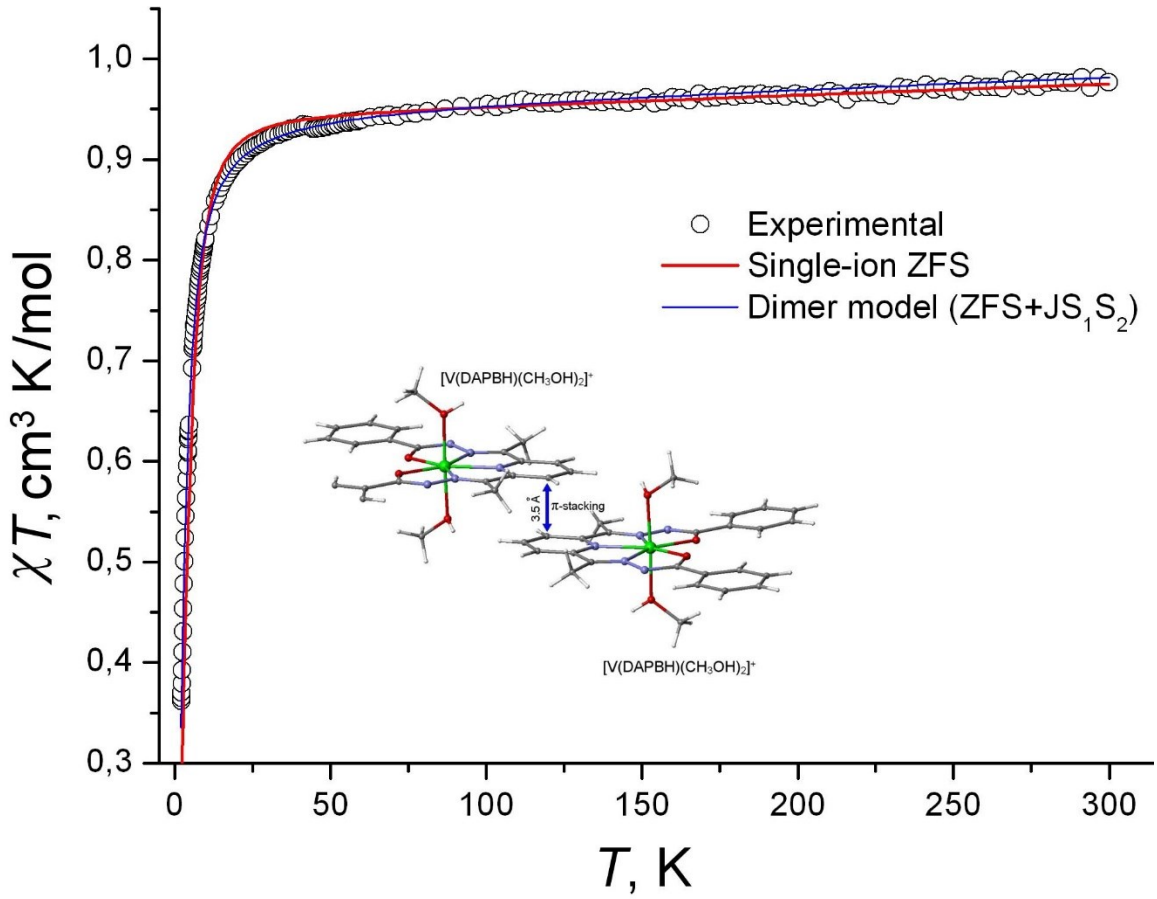

Figure S21. Temperature dependence of the magnetic susceptibility χT of compound **3** (solid blue line) simulated with Eq. (S21) in terms of the dimer-like model with the set of parameters J =–1.1 cm^{-1}, D = +4.6 cm^{-1}, E = 0, g = 1.950, χ_{TIP} = 1.12·10^{-4} cm^3/mol. The relatively strong AF spin coupling in **3** originates from the V(III)-V(III) pair 2 composed of two [V(DAPBH)(CH$_3$OH)$_2$]$^+$ units contacting via π-stacking of planar DAPBH ligands separated by ~3.5 Å (shown in the plot). The χT product of **3** simulated in terms of the single-ion ZFS model (D = +10.1, E = 0.4 cm^{-1}, g = 1.950, χ_{TIP} = 1.12·10^{-4} cm^3/mol) is shown in solid red line.

References

[1] M. Llunell, D. Casanova, J. Cirera, P. Alemany, S. Alvarez, 'SHAPE: Program for the Stereochemical Analysis of Molecular Fragments by Means of Continuous Shape Measures and Associated Tools', Version 2.1, 2013, Barcelona

[2] R. Beaulac, P.L.W. Tregenna-Piggott, A.-L. Barra, H. Weihe, D. Luneau, C. Reber, *Inorg. Chem.* **2006**, *45*, 3399-3407.

[3] (a) Jorgensen, C.K.; Pappalardo, R.; H.H. Schmidtke, *J. Chem. Phys.* **1963**, *39*, 1422-1430; (b) C.E. Schaffer, *Struct. Bonding.* **1968**, *5*, 68-95.

[4] V.S. Mironov, L.F. Chibotaru, A. Ceulemans, *Phys. Rev. B.* **2003**, *67*, 014424–014428.

[5] (a) E.N. Zorina, N.V. Zauzolkova, A.A. Sidorov, G.G. Aleksandrov, A.S. Lermontov, M.A. Kiskin, A.S. Bogomyakov, V.S. Mironov, V.M. Novotortsev, I.L. Eremenko, *Inorg. Chim. Acta.* **2013**, *396*, 108-118; (b) D.G. Samsonenko, C. Paulsen, E. Lhotel, V.S. Mironov, K.E. Vostrikova, *Inorg. Chem.* **2014**, *53*, 10217-10231; (c) V.S. Mironov, *Inorg. Chem.* **2015**, *54*, 11339-11355.

[6] *http://www.op.titech.ac.jp/lab/mori/EHTB/EHTB.html.*

[7] S. Lee, *J. Am. Chem. Soc.* **1989**, *111*, 7754–7761.